

van der Putten, M. A., MacKenzie, L., Davies, A., Fernandez-Ramos, J., Desai, R., Smith, K., and Harvey, A. (2017) A multispectral microscope for in vivo oximetry of rat dorsal spinal cord vasculature. *Physiological Measurement*, 38(2), 205. (doi:[10.1088/1361-6579/aa5527](https://doi.org/10.1088/1361-6579/aa5527))

This is the author's final accepted version.

There may be differences between this version and the published version. You are advised to consult the publisher's version if you wish to cite from it.

<http://eprints.gla.ac.uk/133386/>

Deposited on: 02 February 2017

A multispectral microscope for *in vivo* oximetry of rat dorsal spinal cord vasculature

Marieke A van der Putten¹, Lewis E MacKenzie^{1,2}, Andrew L Davies³, Javier Fernandez-Ramos¹, Roshni A Desai³, Kenneth J Smith³ and Andrew R Harvey¹

¹ School of Physics and Astronomy, University of Glasgow, Glasgow, United Kingdom

² School of Biomedical Sciences, University of Leeds, Leeds, United Kingdom

³ Department of Neuroinflammation, University College London Institute of Neurology, London, United Kingdom

Email: Andy.Harvey@Glasgow.ac.uk

Abstract

Quantification of blood oxygen saturation (SO₂) *in vivo* is essential for understanding the pathogenesis of diseases in which hypoxia is thought to play a role, including inflammatory disorders such as multiple sclerosis (MS) and rheumatoid arthritis (RA). We describe a low-cost multispectral microscope and oximetry technique for calibration-free absolute oximetry of surgically exposed blood vessels *in vivo*. We imaged the vasculature of the dorsal spinal cord in healthy rats, and varied inspired oxygen (FiO₂) in order to evaluate the sensitivity of the imaging system to changes in SO₂. The venous SO₂ was calculated as $67.8 \pm 10.4\%$ (average \pm standard deviation), increasing to $83.1 \pm 11.6\%$ under hyperoxic conditions (100% FiO₂) and returning to $67.4 \pm 10.9\%$ for a second normoxic period; the venous SO₂ was $50.9 \pm 15.5\%$ and $29.2 \pm 24.6\%$ during subsequent hypoxic states (18% and 15% FiO₂ respectively). We discuss the design and performance of our multispectral imaging system, and the future scope for extending this oximetry technique to quantification of hypoxia in inflamed tissue.

Keywords: multispectral imaging, oximetry, spinal cord vasculature

1. Introduction

Tissue hypoxia is associated with inflammation in a range of diseases (Eltzschig & Carmeliet, 2011), including rheumatoid arthritis (RA) (Taylor & Sivakumar, 2005), and inflammation of the central nervous system such as occurs in multiple sclerosis (MS) (Davies, et al., 2013) (Desai, et al., 2016). Measurement of blood oxygen saturation in the vasculature can provide valuable information as to the oxygenation state of the tissue (Beach, 2014). Multispectral imaging (MSI) has become established as a method for vascular oximetry, with a diverse variety of *in vivo* applications including non-invasive retinal oximetry (Mordant, et al., 2011; Choudhary, et al., 2013), ocular microvascular oximetry (MacKenzie, et al., 2016), and investigation of tumour hypoxia in mouse models (Sorg, et al., 2005). The principle of MSI vascular oximetry is based upon the oxygen-dependent optical absorption of haemoglobin, which is the dominant absorber of light in blood. Figure 1 shows the molar extinction coefficients of oxygenated and deoxygenated haemoglobin (values from Prahl, 1999). Unlike techniques for tissue oximetry such as Near-Infrared Spectroscopy (NIRS) which use diffuse transmission measurements through tissue (Murkin & Arango, 2009), in vascular oximetry blood vessels are imaged directly. It is thus possible with vascular oximetry to obtain oxygen saturation

measurements localised to individual blood vessels – something that is not possible with other oximetric techniques such as NIRS.

Vascular oximetry using MSI involves estimation of the absorbance of blood vessels at various oxygen-insensitive (isosbestic) and oxygen-sensitive wavelengths. The optical density of a blood vessel can be empirically related to SO_2 , provided there are known reference values for *in vivo* blood oxygenation, obtained through prior calibration (e.g. two-wavelength oximetry in the retina (Beach, et al., 1999)). Unfortunately, for many applications where localised oximetry *in vivo* is desirable, there are no known reference values as the local environment is highly variable. Absolute calibration-free oximetry may be achieved however, by determining transmission of light through a blood vessel, imaged at multiple wavebands, and fitting the measured transmission values to a theoretical optical model. The model we employ here is based upon the modified Beer-Lambert law, and includes optical absorption, scattering, and other parameters. In this study we applied a multispectral oximetry algorithm which builds upon previous work by others, predominantly for retinal oximetry (Schweitzer, et al., 1995) (Smith, et al., 2000). In addition, we introduce a new contrast-reduction parameter to account for losses of contrast, which can be caused by minor amounts of tissue overlying blood vessels and neighbouring tissue (see Section 2.3). It also compensates for loss of image contrast caused by the modulation transfer function of the imaging system.

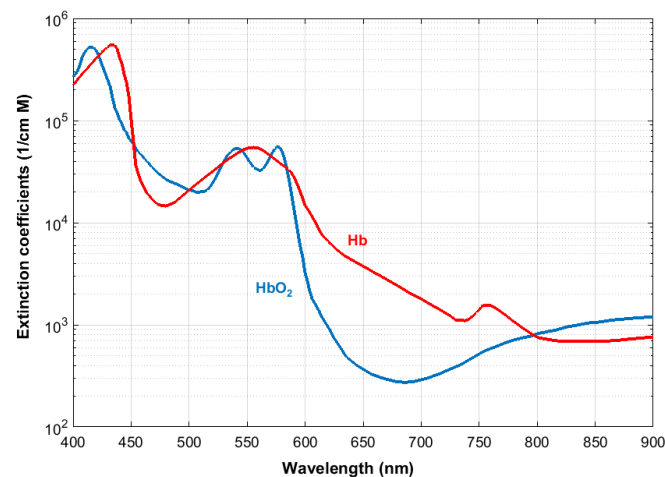


Figure 1. Molar extinction coefficients of oxygenated (HbO_2) and deoxygenated haemoglobin (Hb) as a function of wavelength (Prahl, 1999).

To date, the SO_2 dynamics of the rat spinal cord dorsal veins have not been thoroughly investigated, with only a few limited studies conducted. Figley et al. (2013) reported use of a commercial two-wavelength photoacoustic tomography (PAT) imaging system to monitor a temporary decrease of the dorsal vein SO_2 in rats during hypoxia, however the method for calibration of the PAT device is not reported. Lesage et al. (2009) and Sharma et al. (2011) studied the use of optical imaging and non-imaging light-reflectance spectroscopy respectively, to monitor changes in concentration of oxyhaemoglobin in the rat spinal cord in response to electrical stimulation. Absolute SO_2 values were not reported, however.

Here we introduce a multispectral imaging system suitable for *in vivo* oximetry, and a complementary multispectral oximetry algorithm. The imaging system was designed and assembled using low cost, off-the-shelf optical components. We present results of measurement of venous SO_2 in the dorsal spinal cord vasculature of anaesthetised healthy control rats during normoxia (21% fraction of inspired oxygen [FiO_2]), hyperoxia (100% FiO_2), and hypoxia (18% and 15% FiO_2). This is an easily

transferable technique, and we believe the approach presented in this paper could be applied to the *in vivo* study of a variety of experimental models in which hypoxia is thought to play a role.

2. Methods

2.1. Multispectral microscope

A schematic of the multispectral microscope is displayed in Figure 2. The microscope was designed such that the back focal length of the objective allowed sufficient working space for access to the exposed spinal cord of a rat under general anaesthesia. The microscope also enabled room for surgical equipment and was portable so as to be transferred between labs if necessary. A low-magnification, wide field-of-view system was implemented enabling oximetry of blood vessels across a range of diameters, and multispectral images between 546 nm and 600 nm were acquired.

Illumination was provided by a white LED (*MWWHL3*, *Thorlabs*) with a collimator lens of focal length 40.0 mm (*COP-5A*, *Thorlabs*). An additional lens (*LA1509*, *Thorlabs*, $f = 100$ mm) served as a condenser lens for the illumination path. The LED was controlled by a 4-channel driver (*DC4100*, *Thorlabs*). A liquid crystal tuneable filter (LCTF) (*VIS-7-HC-20*, *Varispec*) provided electronically-controllable spectral discrimination in 1 nm steps between 400 and 700 nm, with spectral full-width at half maximum of 8 nm. Orthogonal polarisation imaging was used to null specular reflections from blood vessels. In consequence the intensity profile obtained from images of the blood vessels arises from light that has been depolarised by multiple scattering within the spinal cord and blood vessels. The analysis described in section 2.2 therefore neglects specularly reflected light, using the ratio of the light intensity either side of the blood vessel to the intensity at the centre of the vessel to estimate Beer-Lambert law attenuation of light transmitted through the blood vessel. This polarisation configuration was achieved by placing a linear polariser (*LPVISE200-A*, *Thorlabs*) in the illumination path oriented to be orthogonal to the polarisation axis of the LCTF.

A single lens reflex (SLR) served as the microscope objective (AF Nikkor f/1.8, $f = 50$ mm), and was configured for finite conjugate imaging. The position of the SLR lens could be manually translated along the z-axis for adjustment of focus. A digital SLR camera (*D300s*, *Nikon*) was used as the detector.

Images were saved as 14-bit RGB NEF (RAW) format and converted to uncompressed greyscale TIFF images for analysis. Greyscale conversion involved selecting either the red or the green channel of the sensor and subtracting the respective dark current channel. The choice of red or green channel was made for each waveband based on which provided higher SNR at that waveband; the red channel was used for $580 \leq \lambda \leq 600$ nm, and the green channel for $546 \leq \lambda \leq 570$ nm. Image acquisition rate was limited by the USB camera interface, which transferred RAW images at a rate of one image every 7.5 seconds; thus a 6-band multispectral dataset was acquired in approximately 45 seconds total. The SLR CMOS detector had 4288 x 2800 pixels and was 23.6 mm by 15.8 mm. The field of view of this configuration was approximately 3.69 mm by 2.47 mm, giving a magnification factor of 6.4 corresponding to 0.88 μ m per pixel. Automated control of illumination, spectral filtering, and image acquisition was achieved using a custom LabVIEW interface.

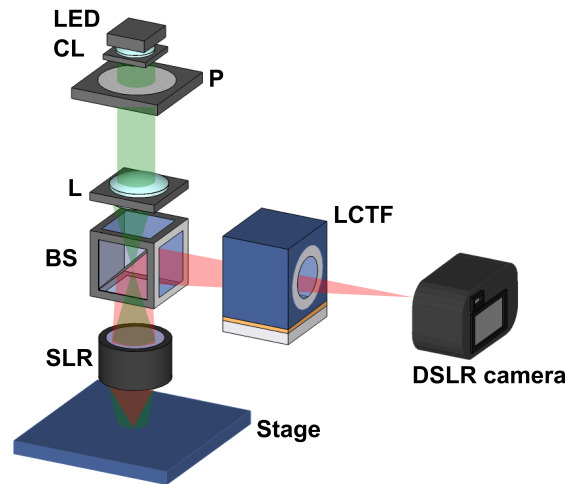


Figure 2. Schematic of multispectral microscope. LED: light emitting diode; CL: collimating lens; P: linear polariser; L: condenser lens; BS: beamsplitter; LCTF: liquid crystal tuneable filter; SLR lens is oriented with back focal plane towards the target. The illumination path is shown in green, and the imaging path in red.

2.2. Multispectral image processing and determination of optical transmission

Six wavebands were selected for imaging: 546, 560, 570, 584, 590 and 600 nm. Sensitivity to changes in SO_2 was provided by the 560 nm, 590 nm and 600 nm wavebands. The 546 nm, 570 nm and 584 nm wavebands were isosbestic, i.e. their absorptions are oxygen-insensitive (see Figure 1). These wavebands provided close to optimal transmission for oximetry in vessels approximately 100 μm in diameter. Accurate oximetry is possible for $0.1 < T < 0.7$ (Smith, 1999), where T is the proportional transmission of light propagated through the blood vessel. Wavelengths longer than 600 nm are unsuitable, as light of this wavelength is weakly absorbed by oxygenated haemoglobin, resulting in low contrast and hence sub-optimal transmission for accurate oximetry. For example, illumination of a 100 μm blood vessel at 700 nm results in optical transmission values of 0.71 and 0.68 for oxygenated and deoxygenated haemoglobin respectively (as calculated using the beer-lambert law), which illustrates the poor contrast between oxygenation states at this wavelength. Wavelengths below 546 nm have poor signal-to-noise ratio due to the low intensity of the LED and the low transmission of the LCTF at these wavelengths, and as such were also deemed unsuitable.

All image processing was implemented using custom algorithms in MATLAB. Images at each waveband were co-registered to form a 6-waveband multispectral data-cube. Vessels were tracked semi-automatically using user-defined control points. A vessel-profile fitting algorithm (see Figure 3) was used to estimate vessel diameter at each waveband at each point along the veins. Diameter estimation was based on the technique described by Fischer et al. (2000); this algorithm determines edges of the vessel as the points of greatest gradient in the 546 nm line profile. From this, the diameter of a vessel in pixels, and hence diameter in microns, could be determined. Transmission of vessels at each wavelength was then determined by a second vessel fitting algorithm. To estimate background intensity (I_o), a linear fit (the red dashed line in Figure 3B) was applied to points of the line profile adjacent to the vessel. A second-order polynomial was fitted to the profile inside the vessel to estimate the intensity at the centre of the vessel (I) (the black dashed line, Figure 3B). The transmission (T) of the vessel was then calculated by $T = \left(\frac{I}{I_o}\right)$.

Only vessels meeting the following inclusion criteria were selected for tracking and oximetry analysis:

1. Vessels with diameter between 50 and 130 μm .
2. Vessels producing a transverse line profile at least three times their diameter, and free of any adjacent vessels, to avoid systemic error in optical transmission calculation.
3. Vessels without taper - e.g. due to curvature around the spinal cord tissue.

Typically only one or two vessels per rat met these inclusion criteria.

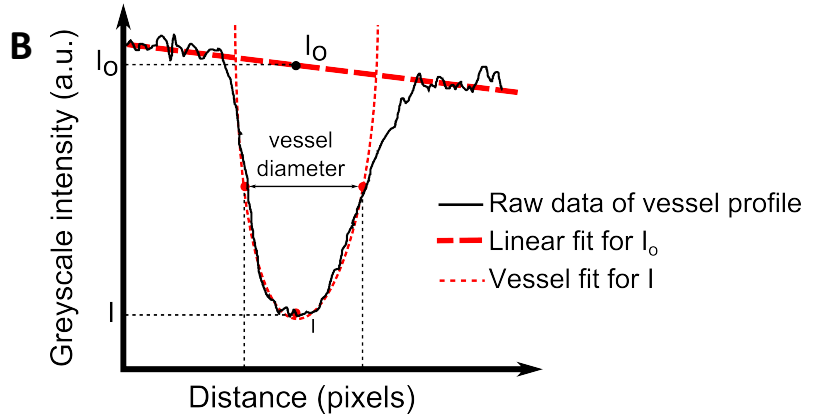
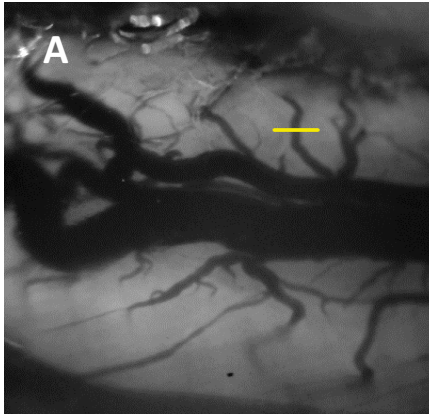


Figure 3. (A) Schematic of line profile along a spinal cord vessel – many such line profiles are taken along each vessel for analysis. **(B)** Illustration of vessel fitting algorithm used to determine vessel diameter and estimate transmission of light at each waveband. *2.3. Oximetry algorithm*

A multispectral oximetry algorithm based on the work of Smith et al. (2000) was developed to estimate SO_2 from transmission values of blood vessels. This algorithm fits a theoretical model of vessel transmission to experimentally measured transmission values, yielding an estimation of SO_2 and related optical parameters. The original model was validated by comparison to femoral artery blood-gas measurements in swine (Smith et al, 2000). The theoretical model predicts the wavelength-dependent transmission of a blood vessel of known diameter by accounting for blood oxygen saturation and incorporating empirical values for extinction and reduced scattering coefficients reported in the literature (Prahl, 1999; Faber et al., 2004; Bosschaart et al., 2014). Further, we add an extra “contrast reduction” parameter– to compensate for local, minor variations in tissue thickness overlying vessels. This tissue tends to add a scattering component which reduces vessel contrast and hence transmission values, leading to incorrect estimation of SO_2 . This section briefly describes how the model was derived.

From the Beer-Lambert law of optical transmission and absorption, we first defined the optical density (OD) of a blood vessel as:

$$OD = \log_{10}(T) = \varepsilon(\lambda)C_{HbT}d, \quad (1)$$

where $T \left(T = \frac{I}{I_0} \right)$ is the experimentally measured transmission of a vessel as depicted in Fig. 3, d is the vessel diameter, C_{HbT} is the molar concentration of total haemoglobin, and $\varepsilon(\lambda)$ is the effective optical extinction coefficient of haemoglobin; $\varepsilon(\lambda)$ is dependent on both the oxygen saturation and wavelength-dependent molar extinction coefficients $\varepsilon_{HbO_2}(\lambda)$ and $\varepsilon_{Hb}(\lambda)$ of oxygenated and deoxygenated haemoglobin respectively. The ratio T is in essence an estimate of the ratio of the light transmitted through the blood vessel to the intensity of light that would have been scattered from the location of the vessel centre in the absence of the vessel. This ratio is thus insensitive to variations in source spectral intensity and the precise optical characteristics of the spinal cord. As discussed below,

the light intensity at the centre of the vessel is due to two dominant components: single-pass light arising from light that has diffused laterally to back illuminate the blood vessel and a double-pass component light that is transmitted through the vessel, scattered from the spinal cord and reflected back through the vessel. A third component due to direct back scatter from the vascular blood is insignificant at these wavelengths and can be neglected. When this technique is used in the retina the presence of variable amounts of pigment (melanin, retinal pigment) means that the relative magnitudes of these components vary within and between retinas. Due to the low level of pigmentation in the spinal cord it is expected that the single-pass transmission is dominant (the tissue point-spread function is much larger than the diameter of the blood vessel) and there should be low variability between and within spinal cords. We used accepted values from the literature shown in Figure 1 (Prahl, 1999). These values are derived from human blood, but it has been shown that the difference between the absorption of light by haemoglobin in rats and humans is minimal (Zijlstra, et al., 1994). Defining c_1 and c_2 as proportional concentrations of oxygenated (HbO₂) and deoxygenated (Hb) haemoglobin respectively, (1) is rewritten as

$$OD = (\varepsilon_{HbO_2}(\lambda) c_1 + \varepsilon_{Hb}(\lambda) c_2) d \quad (2)$$

where: $c_1 + c_2 = C_{HbT}$, so $c_1 = C_{HbT}SO_2$ and $c_2 = C_{HbT}(1 - SO_2)$, and SO_2 is the oxygen saturation; in other words, the proportion of oxygenated haemoglobin in the total solution of haemoglobin. It was also necessary to introduce a parameter to account for attenuation due to optical scattering by blood. Equation (2) is thus rewritten as:

$$OD = C_{HbT} d \left[(\varepsilon_{HbO_2}(\lambda) - \varepsilon_{Hb}(\lambda)) SO_2 + \varepsilon_{Hb}(\lambda) \right] + \mu'(\lambda) d \quad (3)$$

where the $\mu'(\lambda)$ is the wavelength-dependent reduced scattering coefficient, which considers wavelength-dependent scattering (Faber, et al., 2004). By using compiled average values of scattering coefficients $\mu(\lambda)$ and scattering anisotropy factors $g(\lambda)$, we determined these reduced scattering coefficients: $\mu'(\lambda) = \mu(\lambda)(1 - g(\lambda))$ (Bosschaart, et al., 2014).

Two parameters, α and β , are also introduced to account for the combination of single-pass transmission and double-pass transmission as described above. This concept is based on Smith, et al., (2000) and was further validated by Monte Carlo modelling in Hammer et al. (2001) and Rodmell et al. (2014). There will also be a component of transmission which results from direct back-scattering of incident light from the vessel surface, however we omit this due to our illumination configuration employing crossed polarisers. Equation (3) is then rewritten in terms of transmission as:

$$T(\lambda) = \left(\alpha 10^{-\left(C_{HbT} d \left[(\varepsilon_{HbO_2}(\lambda) - \varepsilon_{Hb}(\lambda)) SO_2 + \varepsilon_{Hb}(\lambda) \right] + \mu'(\lambda) d \right)} + \beta 10^{-\left(2 C_{HbT} d \left[(\varepsilon_{HbO_2}(\lambda) - \varepsilon_{Hb}(\lambda)) SO_2 + \varepsilon_{Hb}(\lambda) \right] + 2 \mu'(\lambda) d \right)} \right) \quad (4)$$

Finally, it was considered that various factors other than SO_2 may alter the measured transmission values, such as scattering by overlying tissue. The imaging system itself may also introduce scattering and hence a loss of contrast. Contrast reduction was incorporated as an increase in greyscale intensity I_c of both the background and the vessel. Transmission was hence re-defined as $T'(\lambda) = \left(\frac{I + I_c}{I_o + I_c} \right)$. A contrast parameter K was introduced such that $K = \frac{I_c}{I_o + I_c}$. By substitution, this yields: $T'(\lambda) = T(\lambda)(1 - K) + K$. Applying this substitution to (4), a final model for transmission was derived:

$$T'(\lambda) = \left(\alpha 10^{-\left(C_{HbT}(\lambda) d \left[\left(\epsilon_{HbO_2}(\lambda) - \epsilon_{Hb}(\lambda) \right) SO_2 + \epsilon_{Hb}(\lambda) \right] + \mu'(\lambda) d \right)} + \beta 10^{-\left(2 C_{HbT}(\lambda) d \left[\left(\epsilon_{HbO_2}(\lambda) - \epsilon_{Hb}(\lambda) \right) SO_2 + \epsilon_{Hb}(\lambda) \right] + 2 \mu'(\lambda) d \right)} \right) (1 - K) + K. \quad (5)$$

The experimentally measured transmissions (obtained as detailed in section 2.2) are then fitted to the theoretical model of light transmissions (Eq. (5)) using a nonlinear least-squares fit, yielding estimations of free parameters α , β , K , and SO_2 . A trust region reflective algorithm was employed to perform this least-squares fit. Additionally, vessel diameter was allowed to vary from the measured vessel diameter by $\pm 5 \mu m$. Similarly to SO_2 , the optical parameters α , β and K are all assumed to be invariant over the ~ 55 nm waveband range employed in the illumination scheme. The resulting fits were robust, with SO_2 approximately constant along the vessel. Figure 4 presents an illustrative example of experimentally obtained transmissions along a blood vessel at all six wavebands, and the resulting SO_2 values along the vessel, as produced by the algorithm.

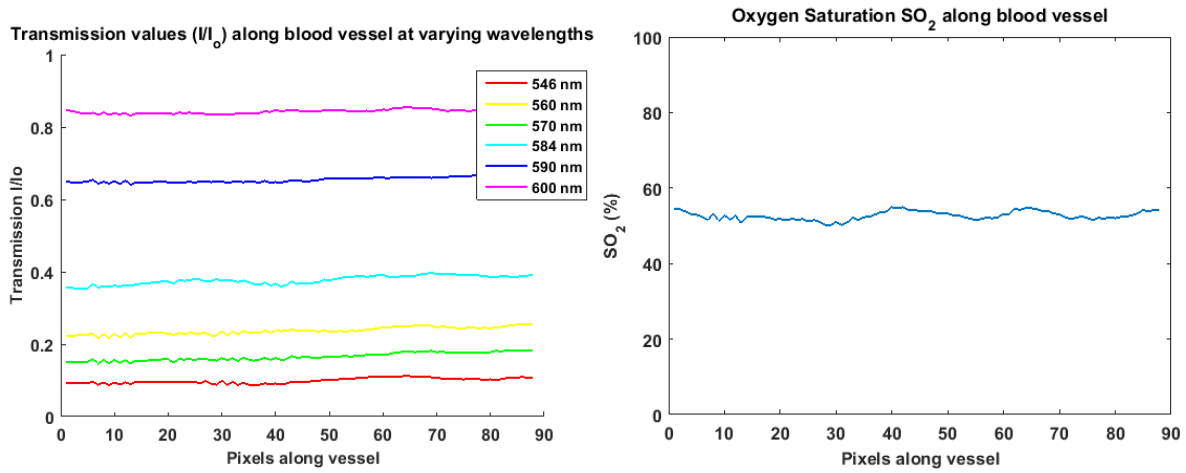


Figure 4. (A) Example of transmission profile along a tributary vessel. **(B)** SO_2 estimated by the multispectral oximetry algorithm along the same vessel.

2.4. *In vivo* imaging procedure

All procedures involving animals were carried out in accordance with the ARRIVE guidelines and the United Kingdom Home Office Animals (Scientific Procedures) Act 1986. Four female Dark Agouti rats (average weight 180 g) were used for the control validation study. A laminectomy was performed under 2% isoflurane anaesthesia in room air, and the dorsal aspect of vertebral segment L1 was removed to expose the cord for imaging. After surgery, the isoflurane was reduced to 1.5% for the remainder of the experiment, including all imaging. Motion due to animal heart-beat and breathing can provide a challenge for *in vivo* imaging, but surgical sutures were used to reduce loading of weight on the rat ribcage and the spinous process rostral to the exposed cord was clamped in place using a modified hemostatic clamp, minimising motion sufficiently for imaging. Similar strategies have been employed in other studies which imaged the murine spinal cord (Johannssen & Helmchen, 2010), (Vinegoni, et al., 2014), (Cadotte, et al., 2012).

Arterial SO_2 was monitored and recorded throughout the experiment using a pulse-oximeter collar (MouseOx, STARR Life). A homeothermic heating mat and rectal temperature probe maintained the rectal temperature at $37^\circ C$. For each rat, image exposure time for each waveband was optimised to ensure sufficient exposure and to avoid image saturation.

Assessing changes in SO_2 due to changes in FiO_2 is an effective and established method for testing the sensitivity of the oximetry technique (Yi, et al., 2015). To assess response to changes in FiO_2 in healthy rats, FiO_2 was varied sequentially, with three full multispectral datasets acquired at each stage of the experiment. The following sequence was used: baseline normoxia (21% FiO_2 for 10 minutes), hyperoxia (100% FiO_2 for 10 minutes), return to normoxia (normoxia 2, 21% FiO_2 for 5 minutes), then incrementally decreasing FiO_2 to induce progressive hypoxia (hypoxia 1, 18% and hypoxia 2, 15%; 5 minutes each). Similar protocols have been used in previous oximetry studies (MacKenzie, et al., 2016), and have been shown to produce a sequence of SO_2 changes that is clearly distinct from normal physiological variation.

3. Results

3.1. Images acquired

Multispectral images were successfully acquired at baseline normoxia 1, hyperoxia, normoxia 2, and hypoxia 1 for all four rats. Rat 1 died before the hypoxia 2 oxygenation state (15% FiO_2), and thus hypoxia 2 data are omitted for this rat. Representative multispectral images of rat spinal cord dorsal vein are shown in Figure 5. The large dorsal vein lies on the dorsal surface of the spinal cord along the rostral-caudal axis, with numerous smaller tributary veins. The large dorsal vein is too absorbing for accurate oximetry, so tributary veins were analysed, provided they met the inclusion criteria described in Section 2.2.

3.2. Response to changes in FiO_2

Average venous SO_2 values are shown in Figure 6. Corresponding arterial values, as measured by the pulse oximeter, are also presented. As expected, average baseline venous SO_2 increased during hyperoxia ($67.8 \pm 10.4\%$ [mean \pm standard deviation] increasing to $83.1 \pm 11.6\%$), and returned to baseline values during the second state of normoxia ($67.4 \pm 10.9\%$) and further decreased during subsequent hypoxic periods ($50.9 \pm 15.5\%$ and $29.2 \pm 24.6\%$ respectively). The differences in average SO_2 between consecutive oxygenation states were all statistically significant ($p < 0.05$, pairwise t-test), with changes between normoxia 1 and hyperoxia, hyperoxia and normoxia 2, and normoxia 2 and hypoxia 1 all highly significant ($p < 0.01$). The normoxia baseline SO_2 values and changes due to FiO_2 interventions are physiologically plausible (normal venous SO_2 is typically $\sim 70\%$), helping to validate our multispectral oximetry algorithm. The results for venous SO_2 for all individual animals are shown in Figure 7 and Table 1. Vessel diameter measurements for all animals are summarised in Table 2, including results of a pairwise t-test between all diameter values at consecutive oxygenation states – which suggested no relationship between measured SO_2 and vessel calibre.

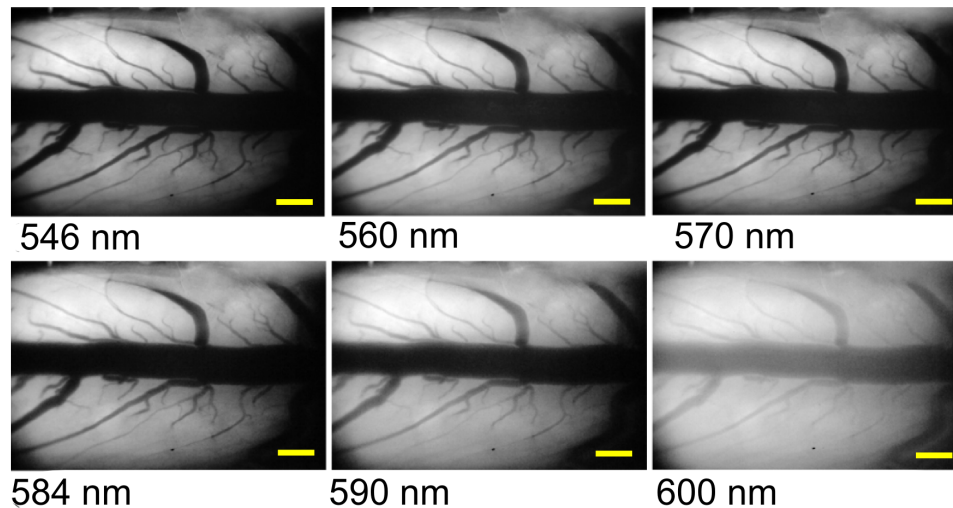


Figure 5. Multispectral images of spinal cord dorsal vein vasculature in a single rat. The main dorsal vein lies on the dorsal surface of the spinal cord, with numerous tributary veins joining the larger vessel. The scale bars represent 500 μm .

3.3. Repeatability and inter-animal variability of measurements

Repeatability of measurements was assessed by performing three measurements of SO_2 at baseline normoxia for each individual rat, where physiological variations are expected to be minimal. The average standard deviation of repeat measurements across all animals was $\pm 2.28\%$ SO_2 . This deviation is much lower than changes in SO_2 observed due to variation of FiO_2 – which was above 15% between normoxia and hyperoxia, and even greater for changes between normoxia and subsequent states of hypoxia. This indicated sufficient repeatability over individual vessels for ascertaining changes in SO_2 .

The changes in venous SO_2 observed throughout the experiment were strongly correlated with changes in arterial SO_2 , as measured by the pulse oximeter. The calculated Pearson correlation coefficients r were 0.74, 0.79, 0.87, and 0.88 for each rat respectively ($p < 0.01$). There was, however, considerable variation in average baseline venous SO_2 between individual rats, ranging from 53% to 78% at normoxia. We did not find a correlation between this variation in venous SO_2 and the baseline arterial SO_2 values. Some physiological variation is expected between rats due to potential differences in depth of anaesthesia and the temperature of the exposed spinal cord (despite maintenance of rectal temperature), both of which may affect venous oxygen saturation.

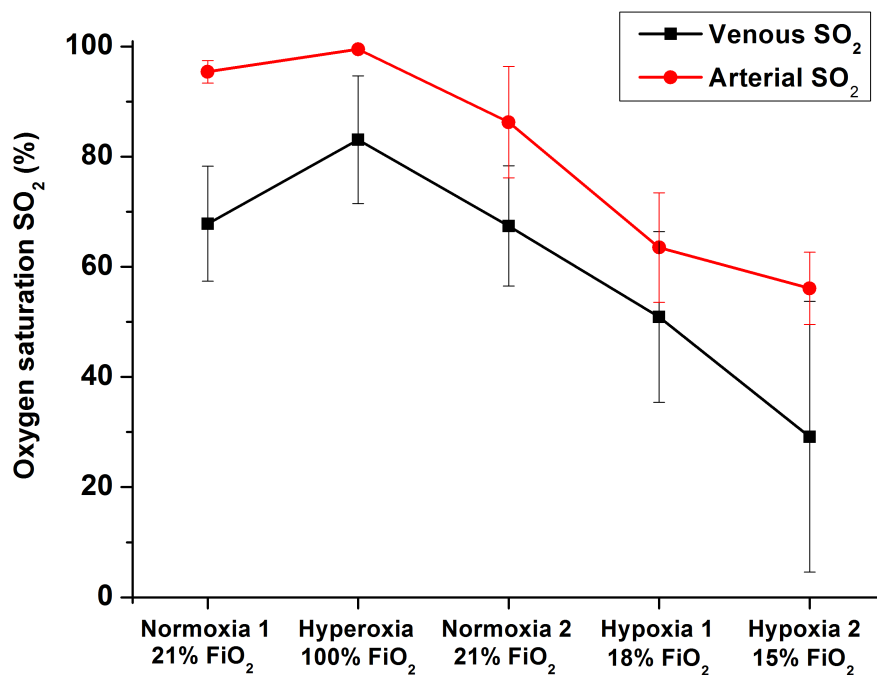


Figure 6. Average venous SO₂ across all animals with variation in FiO₂. Corresponding average pulse oximeter data are also presented. Error bars represent the standard deviation of the average values of each individual rat.

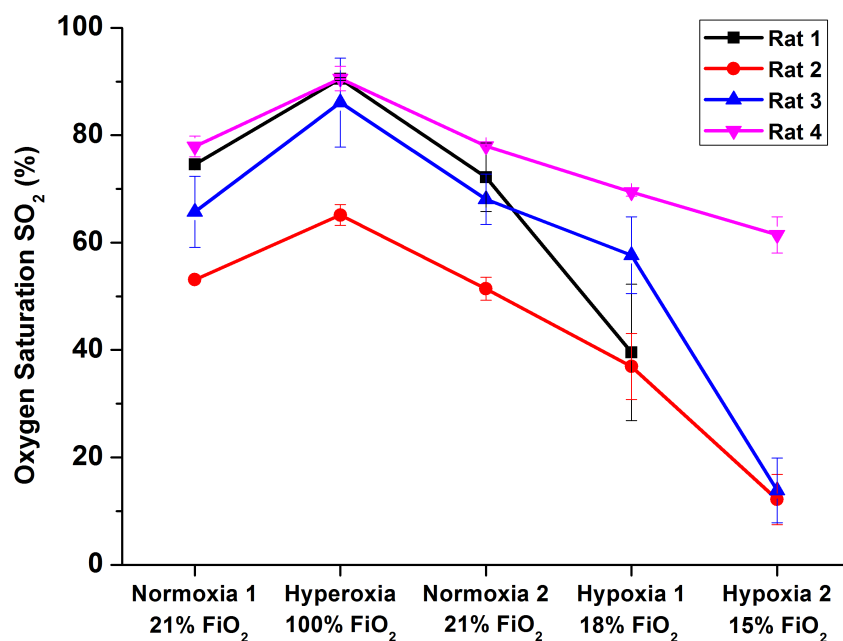


Figure 7. Variation in SO₂ with FiO₂ for each control rat. Results are the average value for each rat \pm standard deviation.

Table 1. SO₂ measurements for individual control rats.

Average rat SO ₂ \pm standard deviation (%)
--

	Rat 1	Rat 2	Rat 3	Rat 4	Average	Change (p-value)
Normoxia 1 (21% FiO ₂)	74.6 ± 0.1	53.1 ± 0.5	65.8 ± 6.6	77.9 ± 1.9	67.8 ± 10.4	n/a
Hyperoxia (100% FiO ₂)	90.5 ± 0.3	65.2 ± 1.93	86.1 ± 8.3	90.6 ± 2.3	83.1 ± 11.6	<0.01
Normoxia 2 (21% FiO ₂)	72.2 ± 6.4	51.4 ± 2.1	68.1 ± 4.7	78.0 ± 0.2	67.4 ± 10.9	<0.01
Hypoxia 1 (18% FiO ₂)	39.6 ± 12.7	36.9 ± 6.2	57.7 ± 7.2	69.4 ± 0.7	50.9 ± 15.5	<0.01
Hypoxia 2 (15% FiO ₂)	N/A	12.2 ± 4.7	13.8 ± 6.00	61.5 ± 3.4	29.2 ± 24.6	<0.05

Table 2. Vessel diameter measurements throughout the experiment.

Average vessel diameter ± standard deviation (µm)					Change (p-value)
	Rat 1	Rat 2	Rat 3	Rat 4	
Normoxia 1 (21% FiO ₂)	104.5 ± 0.9	87.7 ± 0.6	59.5 ± 1.4	100.5 ± 1.1	n/a
Hyperoxia (100% FiO ₂)	108.1 ± 0.6	89.8 ± 1.8	59.3 ± 1.4	103.0 ± 3.3	0.89
Normoxia 2 (21% FiO ₂)	105.5 ± 1.6	87.6 ± 0.7	57.9 ± 5.00	97.7 ± 1.3	0.81
Hypoxia 1 (18% FiO ₂)	107.0 ± 0.7	86.0 ± 0.7	60.8 ± 1.7	99.4 ± 1.4	0.88
Hypoxia 2 (15% FiO ₂)	N/A	81.7 ± 0.6	61.7 ± 1.3	99.3 ± 0.2	0.34

4. Discussion

4.1. Performance of the multispectral microscope

The multispectral microscope provided images of the dorsal vasculature of the rat spinal cord with sufficient magnification and spectral contrast for oximetry of vessels approximately 50 to 130 µm in diameter. Data acquisition was fully automated using a LabVIEW interface to minimise acquisition time and potential human error. Further, the multispectral microscope was assembled with off-the-shelf components, making it a relatively simple and cost-effective device. Using a digital SLR CMOS detector was cost-efficient in comparison with scientific CCD or CMOS detectors, and provided sufficient performance. Further reduction in cost could be achieved by replacing the LCTF with a bank of bandpass filters. The LCTF has the advantage of rapid tuning and adaptability, but LCTF

transmission is low and it is the most costly component of the microscope. A computer-controlled filter wheel would result in slower switching between wavebands, but this would be compensated by shorter integration times afforded by higher optical throughput.

Integration time was less than 1 second for all wavelengths; for the 584 nm, 590 nm and 600 nm wavebands where LCTF transmission is higher, the integration time was as low as 100 ms. Multispectral dataset acquisition rate was limited, however, by the LabVIEW SLR camera control toolbox used (LabVIEW Camera Control for Nikon SLR, *Ackerman Automation*). The resulting data-transfer speed was limited by the USB 2.0 capability of the SLR camera, which limited image acquisition to once every 7.5 seconds. This resulted in an acquisition time of approximately 45 seconds for a multispectral dataset. Acquisition time could be greatly improved in future by using a SLR camera with USB 3.0 capability.

4.2. Performance and validation of oximetry algorithm for *in vivo* imaging

Our oximetry algorithm is based on an algorithm published by Smith et al. (2000). Smith's algorithm was validated in swine by comparing estimations of SO_2 with objective SO_2 measurements obtained by blood-gas analysis of arterial blood from the femoral artery. Further, we have incorporated empirical values of scattering coefficient, anisotropy factor, and extinction coefficients of oxygenated and deoxygenated haemoglobin from the literature, and introduced a novel contrast-reduction parameter to compensate for the optical effects of overlying tissue. Vessel diameter may influence other parameters in our algorithm, such as degree of optical scattering and optical path length of light. In two-wavelength oximetry, for example, it has been reported that large retinal veins are estimated to have a lower blood oxygen saturation than smaller veins (Hammer, et al., 2008), but this may be a vein-diameter dependent calibration artefact in two-wavelength oximetry. We found that fluctuations in diameter for a given vessel between consecutive oxygenation states were not statistically significant (see Table 2), giving confidence that our estimation of SO_2 is independent of blood vessel diameter.

It is clear from measurement that our oximetry analysis provides physiologically plausible values for SO_2 , is sensitive to changes in SO_2 , and is insensitive to vessel diameter. However, highly accurate validation of our oximetry algorithm remains challenging *in vivo*. Whilst the correlations with arterial pulse oximeter data go some way towards explaining the variability in baseline venous SO_2 , verifying the absolute values produced by our technique is difficult. An option for an *in vitro* validation study is to use whole *ex vivo* blood in transparent fluorinated ethylene propylene (FEP) capillaries, placed on a diffuse white reflective background material such as SpectralonTM. *In vitro* validation requires variation of SO_2 in blood, generally achieved by addition of measured quantities of sodium dithionite (Briely-Sabo & Bjornerud, 2000). However, sodium dithionite alters the osmolarity of blood which affects optical properties, including scattering coefficients and anisotropy (Friebel, et al., 2010). The development of a more realistic phantom and an alternative method to artificially deoxygenate whole blood, such as the use of nitrogen gas, would be beneficial and will be considered for future studies (Ghassemi, et al., 2015) (Denninghoff & Smith, 2000).

Many tributary vessels present in the images were too small ($< 50 \mu\text{m}$) to meet our inclusion criteria: such vessels absorb light too weakly for accurate oximetry with the wavelengths used. To enable analysis of smaller vessels, blue wavelengths (at which absorption is higher) could be incorporated into the imaging scheme, providing sufficient contrast for accurate determination of transmission profiles. This would increase the number of veins appropriate for analysis.

5. Conclusions

We have developed a cost-effective multispectral microscope to enable *in vivo*, calibration-free, absolute oximetry of surgically-exposed dorsal veins of healthy rats. SO_2 and vessel diameters of tributary dorsal veins were calculated for a range of inspired oxygen concentrations. This algorithm yielded physiologically plausible values for SO_2 for each rat during normoxia, hyperoxia and graded hypoxia, with SO_2 changing as expected. Further, these results correlated significantly with corresponding arterial SO_2 values as determined by pulse oximetry.

The imaging system and oximetry technique provides sufficient sensitivity to SO_2 such that it may be applied to the study of a variety of disease models where hypoxia may be a factor. The preliminary results presented in this paper suggest that any significant changes in SO_2 related to specific pathological changes will be quantifiable, and it is hoped that future studies using this technique will provide a deeper understanding of disease pathology. The oximetry algorithm developed may be easily extended to a wide range of other applications in future where localised SO_2 measurement is required *in vivo*, such as oximetry in rodent models of multiple sclerosis, rheumatoid arthritis and non-invasive retinal oximetry in humans.

Acknowledgment

This work was funded by the University of Glasgow Sensors Initiative and the Lord Kelvin Adam Smith scholarship programme.

References

- Arango, J. M. a. M., 2009. Near-infrared spectroscopy as an index of brain and tissue oxygenation. *British Journal of Anaesthesia*, Volume 103, pp. i3-i13.
- Beach, J., 2014. Pathway to Retinal Oximetry. *Transl Vis Sci Technol*, 3(5).
- Beach, J. et al., 1999. Oximetry of retinal vessels by dual-wavelength imaging: calibration and influence of pigmentation. *Journal of Applied Physiology*, pp. 748-758.
- Bosschaart, N. et al., 2014. A literature review and novel theoretical approach on the optical properties of whole blood. *Lasers in Medical Science*, Volume 29, pp. 453-479.
- Briely-Sabo, K. & Bjornerud, A., 2000. Accurate de-oxygenation of ex vivo whole blood using sodium Dithionite. *Proc. Intl. Sot. Mag. Reson. Med*, Volume 8, p. 2025.
- Cadotte, D. W. et al., 2012. Speckle variance optical coherence tomography of the rodent spinal cord: in vivo feasibility. *Biomedical Optics Express*, 3(5), pp. 911-919.
- Choudhary, T. R. et al., 2013. Assessment of acute mild hypoxia on retinal oxygen saturation using snapshot retinal oximetry. *Investigative ophthalmology & visual science*, 54(12), pp. 7538-43.
- Davies, A. L. et al., 2013. Neurological Deficits Caused by Tissue Hypoxia in neuroinflammatory disease. *Annals of Neurology*, 74(6), pp. 815-825.
- Denninghoff, K. & Smith, M., 2000. Optical model of the blood in large retinal vessels. *Journal of Biomedical Optics*, 5(4), pp. 371-374.
- Desai, R. et al., 2016. Cause and prevention of demyelination in a model multiple sclerosis lesion. *Annals of Neurology*, 79(4), pp. 591-604.

- 438 Eltzschig, H. & Carmeliet, P., 2011. Hypoxia and Inflammation. *N Engl J Med*, Volume 364, pp. 656-
439 65.
- 440 Faber, D. J. et al., 2004. Oxygen Saturation-Dependent Absorption and Scattering of Blood. *Physics*
441 *Review Letters*, 93(2).
- 442 Figley, S. A. et al., 2013. A Spinal Cord Window Chamber Model for In Vivo Longitudinal Multimodal
443 Optical and Acoustic Imaging in a Murine Model. *PLOS one*, 8(3).
- 444 Friebe, M., Helfmann, J. & Meinke, M. C., 2010. Influence of osmolarity on the optical properties of
445 human erythrocytes. *J. Biomed. Opt.*, 15(5).
- 446 Ghassemi, P. et al., 2015. Rapid prototyping of biomimetic vascular phantoms for hyperspectral
447 reflectance imaging. *Journal of Biomedical Optics*, 20(12).
- 448 Hammer, M., Leistritz, S., Leistritz, L. & Schweitzer, D., 2001. Light Paths in Retinal Vessel Oxymetry.
449 *IEEE Transactions on Biomedical Engineering*, 48(5), pp. 592-598.
- 450 Hammer, M., Vilser, W., Riemer, T. & Schweitzer, D., 2008. Retinal vessel oximetry-calibration,
451 compensation for vessel diameter and fundus pigmentation, and reproducibility. *J. Biomed Opt.*,
452 13(5).
- 453 Johannssen, H. C. & Helmchen, F., 2010. In vivo Ca²⁺ imaging of dorsal horn neuronal populations in
454 mouse spinal cord. *The Journal of physiology*, 588(18), pp. 3397-3402.
- 455 Lesage, F., Brieb, N., Dubeaub, S. & Beaumont, E., 2009. Optical imaging of vascular and metabolic
456 responses in the lumbar spinal cord after T10 transection in rats. *Neuroscience letters*, 454(1), pp.
457 105-109.
- 458 MacKenzie, L., Choudhary, T., McNaught, A. & Harvey, A., 2016. In vivo oximetry of human bulbar
459 conjunctival and episcleral microvasculature using snapshot multispectral imaging. *Experimental Eye*
460 *Research*.
- 461 Mordant, D. et al., 2011. Spectral imaging of the retina. *Eye*, Volume 25, pp. 309-320.
- 462 Pahl, S., 1999. Optical Absorption of Hemoglobin. *Oregon Medical Laser Center*,
463 <http://omlc.org/spectra/hemoglobin/index.html>.
- 464 Rodmell, P. et al., 2014. Light path-length distributions within the retina. *Journal of biomedical*
465 *optics*, 19(3).
- 466 Schweitzer, D. et al., 1995. Calibration-free measurement of the oxygen saturation in retinal vessels
467 of men. *Proc. SPIE, Ophthalmic Technologies V*, 2393(210).
- 468 Sharma, V. et al., 2011. Quantification of light reflectance spectroscopy and its application:
469 Determination of hemodynamics on the rat spinal cord and brain induced by electrical stimulation.
470 *NeuroImage*, 56(3), pp. 1316-1328.
- 471 Smith, M., 1999. Optimum wavelength combinations for retinal vessel oximetry. *Applied optics*,
472 38(1), pp. 258-67.
- 473 Smith, M. H., Denninghoff, K. R., Lompad, A. & Hillman, a. L. W., 2000. Effect of multiple light paths
474 on retinal vessel oximetry. *Applied Optics*, 39(7), pp. 1183-93.

- 475 Sorg, B. S. et al., 2005. Hyperspectral imaging of hemoglobin saturation in tumor microvasculature
476 and tumor hypoxia development. *Journal of biomedical optics*, 10(4).
- 477 Taylor, P. C. & Sivakumar, B., 2005. Hypoxia and angiogenesis in rheumatoid arthritis. *Current*
478 *opinion in rheumatology*, Volume 17, pp. 293-298.
- 479 Vinegoni, C., Lee, S., Feruglio, P. F. & Weissleder, R., 2014. Advanced Motion Compensation Methods
480 for Intravital Optical Microscopy. *IEEE Journal of Selected Topics in Quantum Electronics*, 20(2).
- 481 Yi, J. et al., 2015. Visible light optical coherence tomography measures retinal oxygen metabolic
482 response to systemic oxygenation. *Light: Science & Applications*, 4(e334).
- 483 Zijlstra, W., Buursmaa, A., Falke, H. & Catsburg, J., 1994. Spectrophotometry of hemoglobin:
484 absorption spectra of rat oxyhemoglobin, deoxyhemoglobin, carboxyhemoglobin, and
485 methemoglobin. *Comp. Biochem. Physiol.*, 107B(1), pp. 161-166.
- 486